

Tilt Engineering in Prussian White Cathode $\text{Na}_{1+x}\text{Fe}[\text{Fe}(\text{CN})_6]$ via Mg-doping for Enhanced Electrochemical Performance in Na-ion Batteries

Ashwani Tyagi^[a] and Sreeraj Puravankara^{*[a]}

Due to their robust open framework structure and facile synthesis techniques, Prussian blue analogs (PBAs) can be a suitable and cost-effective cathode for Na-ion batteries. Despite higher sodium content and low defects, the Prussian white (PW) still shows lower reversible capacity due to the limited participation of low-spin Fe and restricted Na-ion diffusion due to non-optimized octahedral tilts. Here, we report improving the electrochemical performance of PW by optimizing the octahedral tilts through Mg doping. The pristine $\text{Na}_{1.8}\text{Fe}[\text{Fe}(\text{CN})_6] \cdot 2.75\text{H}_2\text{O}$ delivers the reversible capacity of 127 mAh g^{-1} with a capacity retention of 69% after 250 cycles. However, 10% Mg-doped samples $\text{Na}_{1.81}\text{Mg}_{0.09}\text{Fe}_{0.81}[\text{Fe}(\text{CN})_6] \cdot 2.58\text{H}_2\text{O}$ de-

liver an improved reversible capacity of 138.2 mAh g^{-1} and capacity retention of 85% after 250 cycles at C/10 rate. By replacing Fe, Mg incorporation into the $\text{Na}_{1+x}\text{Fe}[\text{Fe}(\text{CN})_6]$ framework increases the electron density, which is propagated throughout the –Fe–CN–Fe–NC– chain and weakens the strong CN ligand field. This results in the participation of additional low-spin Fe in the electrochemical reaction. Mg incorporation also provides structural stability by reducing the distortion magnitude and enhancing diffusion kinetics by optimizing the octahedral tilt angle to improve the battery metrics of the cathode.

Introduction

Cathode materials for Na-ion batteries (SIBs) have been extensively explored in the past decade - layered transition metals, phosphate polyanions, pyrophosphate polyanions, fluorophosphate polyanions, NASICON-type polyanion, organic cathodes, and Prussian blue analogs (PBAs).^[1-8] Among the cathodes, PBAs ($\text{A}_2\text{M}[\text{Fe}(\text{CN})_6] \cdot n\text{H}_2\text{O}$, A=Na, K, M=transition metals) have gained significant attention because of their robust open framework structure, facile synthesis method, and economic cost.^[8,9] Despite these advantages, PBA cathodes suffer from defects created during synthesis, interstitial and coordinated water, oxidation of Fe^{2+} to Fe^{3+} during synthesis, and limited participation of low spin Fe into the electrochemical reaction, which requires further structural improvements for its application in the mainstream battery industries. Various efforts have been made to improve the electrochemical performance of the PW cathode. Huang et al. synthesized a low-defect $\text{Na}_{1.95}\text{Fe}[\text{Fe}(\text{CN})_6]_{0.93-0.07} \cdot 3.6\text{H}_2\text{O}$ by co-precipitation method using PVP K-30 surfactant. The cathode delivered 120 mAh g^{-1} @ 50 mA g^{-1} and showed capacity retention of 81.1% after 150 cycles.^[11] Yang and his team developed low-defect PW with a formula $\text{Na}_{1.73}\text{Fe}[\text{Fe}(\text{CN})_6]_{0.98-0.02}$ using the co-precipitation method at different temperatures. They achieved a specific

capacity of 123 mAh g^{-1} @ 100 mA g^{-1} and a capacity retention of 73.4% after 200 cycles.^[12] You et al. developed low Sodium Prussian blue by single iron source method, $\text{Na}_{0.61}\text{Fe}[\text{Fe}(\text{CN})_6]_{0.94-0.06}$. The cathode delivered the specific capacity of 170 mAh g^{-1} @ 25 mA g^{-1} and showed capacity retention of 100% after 150 cycles.^[13] The most important point we can note here is that the reversible capacity of the PBA cathode does not directly depend upon the Sodium content and defects. However, there must be some other physical quantity, which is the convolution of Na-content, defect, and water content, and its synergistic effect influences the electrochemical performance of the PBA cathode. A brief understanding of PBA crystal structure can provide better insight. PBAs are a hybrid perovskite type with a structure similar to the cubic ABX_3 perovskite lattice.^[14] In PBAs, cyanide molecules serve as the X^- anionic component. This molecular component implies that the perovskite enclosure, precisely the space surrounding A^+ cations, is considerably more significant in the case of PBAs than in traditional perovskite ceramics.^[16,17] As a result, the anionic framework becomes more flexible. This flexibility can be responsive to Na-ion content, defects, water content, and pressure.^[17] These responses manifest as lattice distortions, as evident in X-ray studies.^[18] When the stoichiometry of the A-site cation (Na in our case) tends towards its maximum value 2, The electrostatic interaction of the M-site cyanide ligand with the A-site cation results in the structural distortion by tilting the $[\text{FeCN}]_6$ octahedra to form cubic to monoclinic or rhombohedral phase.^[18-20] The interaction between the carrier ion (Na/Li) and anionic ligand $\text{Fe}^{3+}[\text{Fe}^{3+}(\text{CN})_6]$ can influence the redox potential of transition metal ions and phase evolution.^[21-23] I. Hasa et al. studied the effect of dehydration and observed the emergence of the Rhombohedral phase in monoclinic PBA

[a] A. Tyagi, Dr. S. Puravankara
School of Energy Science & Engineering, IIT Kharagpur, Kharagpur -721302,
West Bengal, India
Phone (Office) - +913222 260801
E-mail: sreeraj@iitkgp.ac.in

 Supporting information for this article is available on the WWW under
<https://doi.org/10.1002/batt.202500045>

along with the volume reduction.^[24] Willian R. Brant and his team also observed the volume reduction upon dehydration of PBA.^[25] Despite the main framework being unperturbed, the effect of hydration on volume change needs to be rationally addressed. This observation can be related to octahedral tilt distortion, also known as volume-minimizing distortion. The volume change can also be associated with strain exerted on the host PBA framework, thus directly influencing the cycling performance.^[21] Therefore, Understanding and developing control over the presence and nature of distortion in the PBA can be a crucial aspect of material design in PBA for battery application.^[26,27] The Goldschmidt tolerance factor for predicting the extent of distortion in perovskite can be extended with the PBA materials due to their similar geometry in previous studies.^[28,29] Most theoretical studies are based on the homovalent bridge structure, which accounts for the reduced metal centers. However, the metals are arranged in a multivalence state in low-sodium, low-defect PBAs, making it a syn-anti compound. The transition metals are also present in low-spin state M¹-CN and high-spin state M²-NC (M¹, M²=Transition metal), resulting in different ionic radii of transition metals. The generalization of distortion, in this case, is limited and needs to be addressed for a better understanding.

Herein, refining the Goldschmidt tolerance factor as a tool, we report improving the electrochemical performance of PW by optimizing the octahedral tilts through Mg doping. The optimized 10% Mg-doped samples Na_{1.81}Mg_{0.09}Fe_{0.81}[Fe(CN)₆]·2.58H₂O deliver an improved reversible capacity of 138.2 mAhg⁻¹ and capacity retention of 85% after 250 cycles at C/10 rate. Optimizing the Mg-doping increases the low-spin Fe center capacity contribution, improves the Na-ion diffusion kinetics, and enhances battery metrics as the cathode for SIBs.

Synthesis of Na_{1+x}Fe_{1-y}Mg_y[Fe(CN)₆] (x=0, 0.05, 0.10, 0.15)

Na_{1+x}Fe[Fe(CN)₆] was synthesized through co-precipitation using two solutions, where solution A contains four mmol of Na₄Fe(CN)₆ dissolved in 200 ml of deionized (DI) water. Solution B was made by dissolving six mmol of FeSO₄·7H₂O and 15 grams of tri-sodium citrate in 200 ml of DI water (Scheme S1). Trisodium citrate is a chelating agent that helps us control reaction kinetics and minimize defect formation by slowing down chemical reactions. Solution B was added dropwise to solution A (7 ml/min) under continuous stirring to obtain a white precipitate immediately. After the complete addition of solution B, the stirring was stopped, and the solution was allowed to age for 12 hours. After the aging, the resultant solution was centrifuged (~3500 rpm), filtered, and the precipitate was washed successively with DI and ethanol. The predominately white powder with a tint of cyan was kept in a vacuum oven for 24 hrs at 100°C at 1 bar pressure. The resultant powder was labeled as NFM_0. A similar synthetic procedure was used to synthesize Mg-doped PBA with different amounts of doping concentration. The 5% Mg-doped, 10% Mg-doped, and 15% Mg-doped samples were synthesized with the exact formulation of solution A. However, solution B was

changed for different Mg doping concentrations; 5.7 mmol of FeSO₄·7H₂O and 0.3 mmol of MgSO₄ were taken with 15 grams of trisodium citrate for 5% Mg-doped PBA. For 10% Mg-doped PBA, solution B consists of 5.4 mmol of FeSO₄·7H₂O, 0.6 mmol of MgSO₄, and 15 grams of trisodium citrate. 15% Mg-doped PBA required 5.1 mmol of FeSO₄ and 0.9 mmol of MgSO₄ with 15 grams of trisodium citrate to form solution B. The later steps were followed as described for the synthesis of pristine NFM_0. The 5% Mg, 10% Mg, and 15% Mg-doped PBA were labeled NFM_05, NFM_10, and NFM_15, respectively.

Material Characterizations

The prepared samples' crystalline structure and phase investigation were done by Bruker D2 phaser with a Cu K α X-ray radiation source ($\lambda = 1.54056 \text{ \AA}$). A thermogravimetric (TG) study was carried out by Perkin Elmer Pyris Diamond TG-DTA system in an N₂ flow environment in the temperature range 25–650°C with a scan rate of 10°C/min. The morphology of the samples was obtained using a FEG-SEM (Merlin). The oxidation states and binding energies of all the samples were measured using an X-ray Photoelectron Spectrometer PHI 5000 Versa Probe III. The chemical environment of the samples was mapped using the FTIR (Thermo Fisher Scientific Instruments Nicolet 6700). The Raman Spectroscopy was done (T64000, Jobin Yvon Horiba, France) with an excitation source of Ar-Kr mixed ion gas laser (Spectra-Physics, USA).

Electrochemical Studies

The electrochemical performance of the samples was carried out using a CR2032 coin cell. The working electrode was prepared by 70:20:10 wt% ratio of as prepared material, carbon black and poly(vinylidene fluoride) (PVDF). The mass loading was kept in the 1.25–1.45 mg cm⁻² range. 1 M NaClO₄ in ethylene carbonate (EC) and propylene carbonate (PC) (1:1 v/v) in glass microfiber was used as the electrolyte, and all measurements were carried out at 25°C. The evaluated capacity and battery metrics were calculated based on the mass of the cathode active material. The charge-discharge protocols at varying C-rates were carried out with a Neware battery cycler in the voltage window 2 V–4.2 V (vs. Na⁺/Na). The cyclic voltammetry (CV) (@ 0.1 mV/s) and EIS were recorded (Biologic, France) in the voltage window 2–4.2 V.

Results and Discussion

Figure 1(a), (b), (c), and (d) show Rietveld refined XRD pattern of NFM_0, NFM_05, NFM_10, and NFM_15. All the materials crystallize into a monoclinic structure (space group- P2₁/n). Mg doping in pristine NFM induces lattice parameter changes. The refined lattice parameters of NFM_0, NFM_05, NFM_10, and NFM_15 are tabulated and shown in Table 1. NFM_0 shows $a = 10.4253(11) \text{ \AA}$, $b = 7.3186(11) \text{ \AA}$, $c = 7.3999(17) \text{ \AA}$, $\beta =$

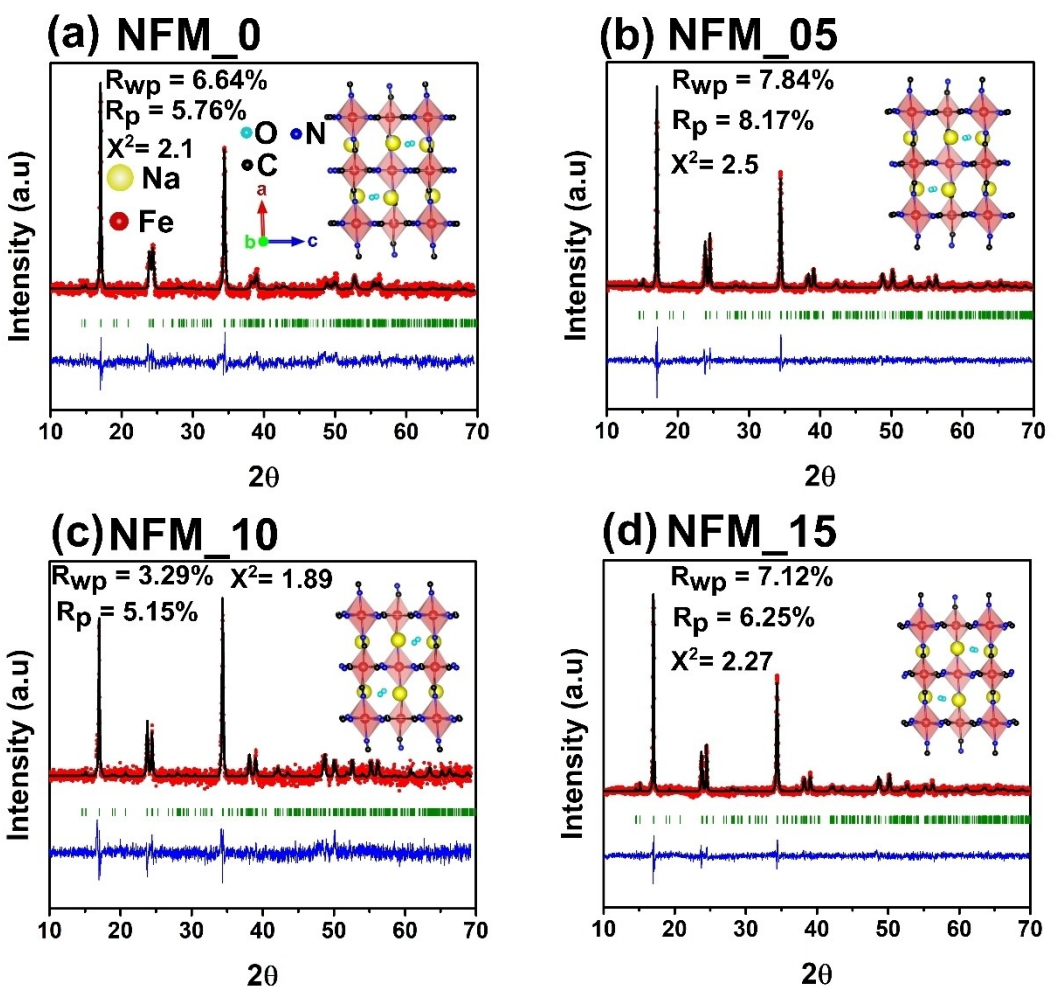


Figure 1. Rietveld refined XRD patterns of (a) NFM_0, (b) NFM_05, (c) NFM_10 and NFM_15 (all the refinement parameters have been summarized in Table S1, S2, S3, S4 and S5.)

Table 1. Lattice parameters of NFM_0, NFM_05, NFM_10, and NFM_15 were obtained from the Rietveld refinement of the XRD diffractogram with monoclinic structure (space group P2₁/n) and coordinated water determined from TGA (Figure S2).

Sample Name	a (Å)	b (Å)	c (Å)	β	Cell Volume (Å ³)	Coordinated water
NFM_0	10.4253(11)	7.3186(11)	7.3999(17)	92.0230(18)	564.2513	16%
NFM_05	10.4387(6)	7.4319(6)	7.2829(5)	92.2720(6)	564.6074	14.62%
NFM_10	10.4464(7)	7.5049(9)	7.2572(9)	92.0090(7)	568.6093	15.21%
NFM_15	10.4434(6)	7.4546(7)	7.2883(6)	92.3920(7)	566.8860	13.73%

92.0230°(18) and cell volume of 564.2513 Å³. NFM_05 have a = 10.4387(6) Å, b = 7.4319(6) Å, c = 7.2829(5) Å, β = 92.2720(6) and cell volume of 564.6074 Å³.

The lattice parameter a = 10.4464(7) Å, b = 7.5049(9) Å, c = 7.2572(9) Å, β = 92.0090(7) and cell volume of 568.6093 Å³ was observed in NFM_10. In case of NFM_15, a = 10.4434(6) Å, b = 7.4546(7) Å, c = 7.2883(6) Å, β = 92.3920(7), and cell volume of 566.8860 Å³. A gradual increase in "a" parameter and cell volume is observed with increased Mg-doping. However, NFM_10 shows deviation from the observed trend; this anomaly is due to lesser tilt distortion due to the combined effect of

optimized Mg-doping and water content, which will be discussed later. In the monoclinic PW structure, the iron centers Fe^{II} and Fe^{III} are octahedrally coordinated with carbon and nitrogen atoms of cyanide ligand forming low-spin (LS) [Fe-C₆] and high-spin (HS) [Fe-N₆] Fe.^[30] Together, these atoms arrange themselves into ABX₃ perovskite-like structures.^[31] Na atoms occupy the inbuilt pores (A-sites) to complete the PW structure. However, water coexists at the A-site in the PW structure (interstitial water).^[32] The anionic framework around the sodium atom possesses substantial flexibility, which can significantly respond to temperature, pressure, change in Na content,

change in water content, and defects in the lattice. These changes manifest in the form of distortion in the monoclinic phase - (i) change in unit cell length, (ii) A-site slide component, and (iii) tilt distortion.^[33,34,35] The change in unit cell length has already been discussed in the previous section. The A-site slide component can be activated in case of low defect and high sodium content. Once the A-site slide is activated, the A-site cation can occupy a lower symmetry site with a narrow potential energy well; a narrower pore size reduces the diffusion kinetics of A-site Na-ion, affecting the cathode performance. Figure 2(a) shows the crystal structure of NFM_0 when glanced from the a-axis using the ball and stick model. The purple ball represents the Na-ions, the cyan ball represents the oxygen in water, and the blue and black balls represent

nitrogen and carbon, respectively. Figure 2(b, c, d) represents NFM_05, NFM_10, and NFM_15, respectively, using wireframe structure. The yellow balls represent Na-ions, and the cyan balls represent oxygen in water; the carbon and nitrogen are on the wire frame. To demonstrate the subtle Na-slide due to Mg doping, Figure 2(b, c, d) have been superimposed with the Na-ion position (in a red dotted circle) from NFM_0 on Figure 2(a) respectively to form Figure 2(e, f, g) with overlapping origins. In Figure 2(e, f, g), the red circle has been used to highlight the sodium atoms in NFM_0 and refined to observe the effect of Mg doping on the Na-slide within the crystal against the pristine NFM_0. In Figure 2(e, f, g), we can observe the Na-ion slide at the A-site with increased Mg doping. The direction of the slide has been marked with a blue arrow; the effect of the

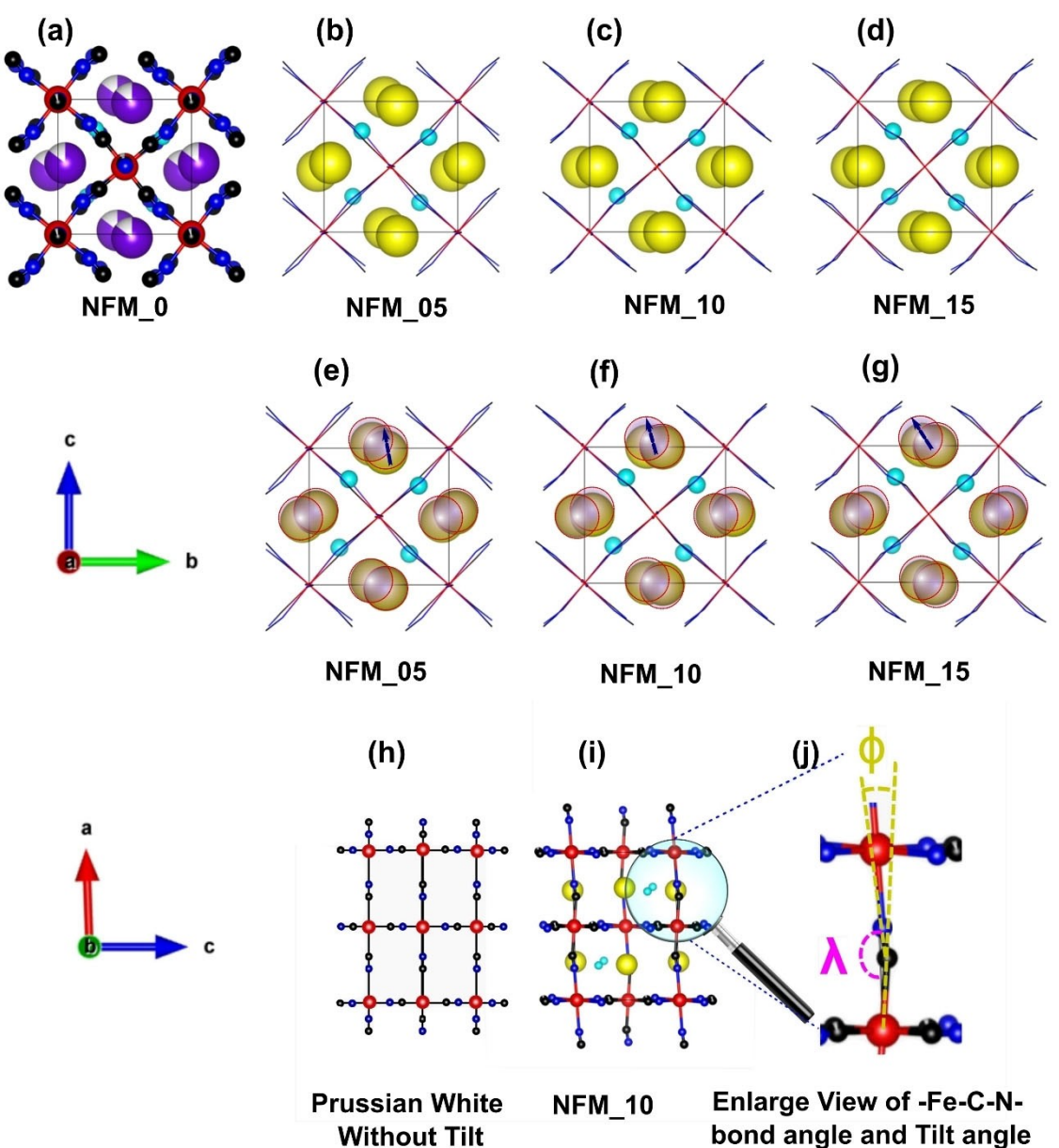


Figure 2. Crystal geometry of NFM samples along a-axis (a) NFM_0, (b) NFM_05, (c) NFM_10, (d) and NFM_15; Superimposed image of Na from NFM_0 (in red dotted circle on ((e) NFM_05, (f) NFM_10 and (g) NFM_15) along a-axis showing Na-slide. (h) Hypothetical Prussian white crystal structure without any tilt, (i) Crystal structure of NFM_10, (j) zoomed image of -Fe-C-N- from figure "i" to demonstrate the -Fe-C-N- angle (λ) and tilt angle (ϕ).

Na-slide direction can further be related to the electrochemical properties of the material. Our analysis of XRD patterns obtained from NFM_0, NFM_05, NFM_10, and NFM_15 displays the presence of tilt distortion in the monoclinic phase of NFM_0, NFM_05, NFM_10, and NFM_15. Ideally, in lower sodium content PBAs with cubic structure, the angle between $-Fe-C-N-$ and $-Fe-N-C$ should be 180° and as PBAs reach the richer Na stoichiometry approaching the maximum possible stoichiometry (~ 2), they undergo octahedral tilt distortion (Figure 2(h, i, j)). This distortion results from the electrostatic attraction between a-site cation and cyanide anion, and the most common tilt pattern observed in monoclinic structures is $a^-a^+b^+$. The Glazer notation defines "+" for in-phase and "-" for out-of-phase tilt^[36] (Figure S6 (d, e, f)). However, this systematic tilting or rigid tilting is strictly followed when two octahedra are directly connected, as in the case of ABX_3 types perovskite structures where the corner is shared in BX_6 octahedra (Figure S6(a, b, c)). In the case of PW $A_2M^1[M^2(CN)_6]$, where M^1C_6 and M^2N_6 octahedra are indirectly connected with a cyanide bridge, therefore making the tilting more flexible (Figure S6 (d, e, f)). If a B-site cation is introduced, which can modify the cyanide bond length, it can activate numerous possible unconventional tilt patterns; therefore, to limit the discussion, the naming of unconventional tilt patterns observed has not been included. The extent of distortion in Perovskite (ABX_3) or perovskite-like structures can be rationalized by the Goldschmidt tolerance factor (α). The modified tolerance factor is given by:^[29]

$$\alpha = \frac{r_A^{eff} + r_X^{eff}}{\sqrt{2}(r_B + 0.5h_X^{eff})} \quad (1)$$

where r_A^{eff} is the effective ionic radius of the A-site cation, the organic ligand cyanide is viewed as a cylinder, and r_X^{eff} and h_X^{eff} represent the effective radius and effective height of the cyanide cylinder and r_B is the effective ionic radii of a divalent cation, as proposed by Shannon.^[37] Here, the value of r_X^{eff} and h_X^{eff} was taken as 1.68 \AA and 3.65 \AA , respectively, as used in previous studies.^[29] The tolerance factor (α) was calculated for NFM_0, NFM_05, NFM_10, and NFM_15, respectively, and summarized in Table S8. The r_B for the samples were taken as the average effective ionic radii of LS- Fe^{2+} and HS- Fe^{2+} , and for Mg-doped samples, the Mg-doping was replaced from HS- Fe^{2+} . The distortion magnitude observed for our samples was calculated as δ .^[28]

$$\delta = \frac{V_{ref} - V_{exp}}{V_{ref}} \quad (2)$$

V_{ref} is the reference volume of undistorted cubic $Na_xFe[Fe(CN)_6]$ with space group Fm-3 m.^[38] V_{exp} is the experimentally observed volume of NFM samples. Empirically expected distortion magnitude as the function of " α " observed by Andrew L. Goodwin and his team is given by:^[28]

$$\delta_{emp} \approx 2(1 - \alpha) \quad (3)$$

The value of α for NFM_0, NFM_05, NFM_10, and NFM_15 was found to be 0.7531, 0.758, 0.7585 and 0.7589, respectively. An increasing trend in the value of α was observed with increased Mg doping. The corresponding expected distortion magnitude of NFM samples δ_{emp} was found to be 0.4938, 0.4840, 0.4830, and 0.4822. A decrease in the value of δ_{emp} is expected with an increase in Mg substitution. The δ_{emp} value represents the magnitude of the volume reduction caused by distortion concerning the undistorted reference cubic lattice; for example, NFM_0 shows $\delta_{emp}=0.4938$, indicating a 49.38% volume reduction compared to the cubic lattice. An increase in Mg doping should reduce the distortion magnitude, leading to expansion in the cell volume, as observed experimentally. The observed distortion magnitude δ for NFM_0, NFM_05, NFM_10, and NFM_15 was found to be 0.488599, 0.488237, 0.484609, and 0.486171, respectively. The increase in Mg doping reduces the distortion magnitude, and the observed values of δ are in close agreement with δ_{emp} within the experimental error. However, NFM_10 deviates from this trend, making it the least distorted structure, and therefore, the maximum volume of 568.6093 \AA^3 was observed among all the NFM samples. The most probable reason for this anomaly can be an increase in the value of α caused by the rise in the value of in equation (1). The value can change when interstitial water is present. In our case, A site cation Na can interact with interstitial water, forming $[Na-OH_2]^+$ and, therefore, creating a larger sphere with an increase in the value of.^[39,40] The other possible reason is the change in the concentration of A-site cation, which will be discussed later. The tilt distortion angle ϕ , defined in equation 4 and represented in (Figure 2(i, j)), was calculated using the data in Table S5 :

$$\phi = 180^\circ - \lambda \quad (4)$$

(λ is the average angle between $-Fe-C-N-$ and $-Fe-N-C-$)^[41] ϕ for NFM_0, NFM_05, NFM_10, and NFM_15 was found to be 7.97° , 13.42° , 10.69° , and 14.96° respectively. A gradual increase in octahedral tilt angle can be observed with Mg doping. However, a deviation from the linear trend was observed in NFM_10 due to other competing effects of interstitial water. FTIR spectra (Figure 3(a)) show peaks at 3624 cm^{-1} , 3540 cm^{-1} , and 1613 cm^{-1} in all the samples, corresponding to the presence of water. No significant change was observed in the bending mode of Fe–O at $\sim 460\text{ cm}^{-1}$ and $-Fe-C\equiv N-Fe-$ at $\sim 600\text{ cm}^{-1}$.^[42] Further, the water content was quantified using TGA (Figure 3(c, d, e, f)). The water content (wt%) for NFM_0, NFM_05, NFM_10, and NFM_15 was found to be 16%, 14.62%, 15.21%, 13.73%. The higher water content in NFM_10 compared to other Mg-doped samples leads to an increase in the value of r_A^{eff} of A-site cation, which reduces the distortion magnitude, the least volume contraction, and lesser tilt to stabilize the structure was observed.^[43] Raman spectroscopy was performed (Figure 3(b)) to clarify the possibility of sodium content contributing to the structure's octahedral tilt. The peaks were observed at 2135 cm^{-1} , 2115 cm^{-1} , and 2098 cm^{-1} for all the samples; no significant shift was observed, confirming the same amount of sodium in all the samples, as from the earlier

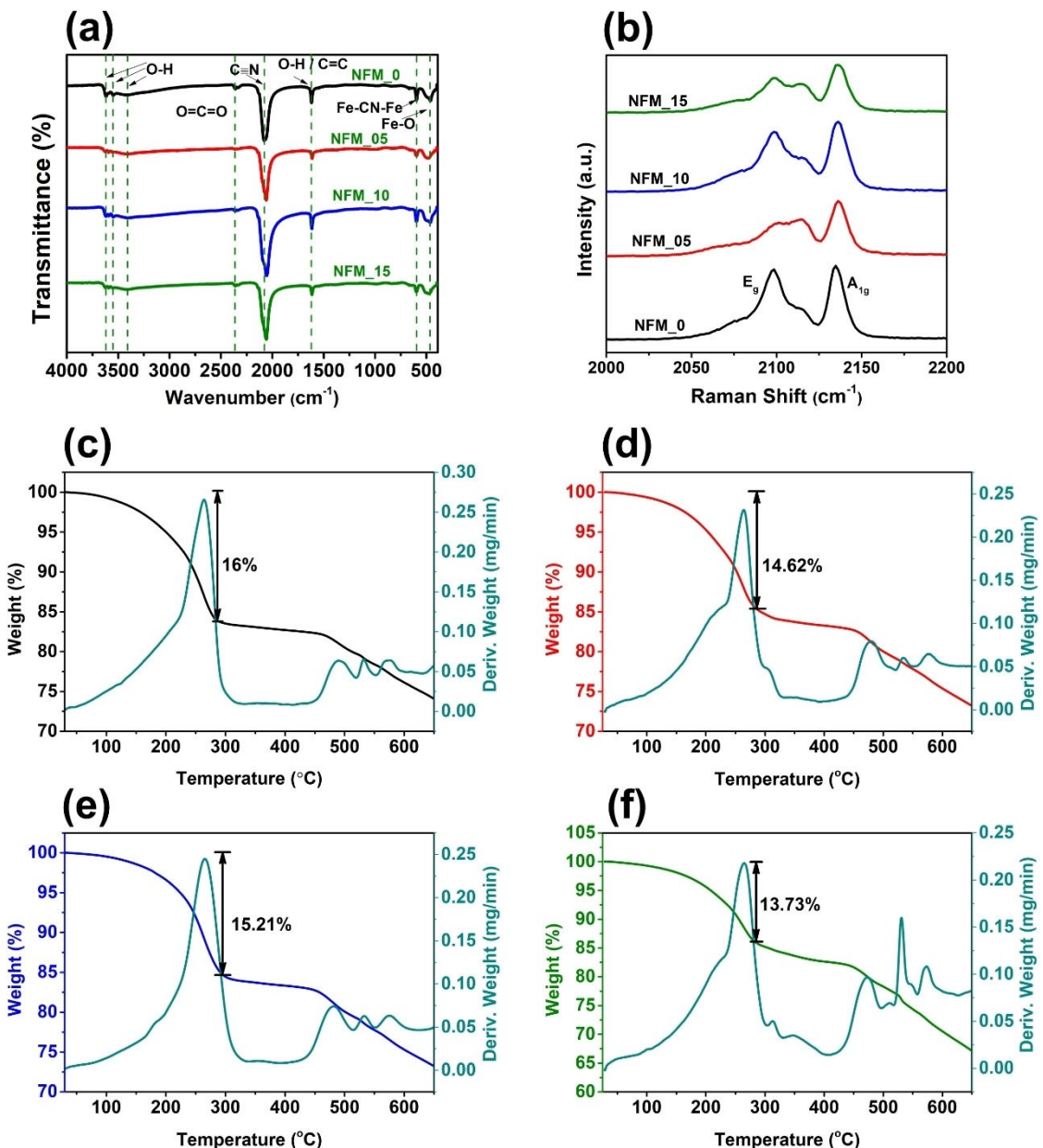


Figure 3. (a) FTIR spectral profiles of NFM_0, NFM_05, NFM_10 and NFM_15 (b) Raman spectral profiles of NFM_0, NFM_05, NFM_10, and NFM_15; TGA image of: (c) NFM_0, (d) NFM_05, (e) NFM_10 and (f) NFM_15

reports, the cyanide stretching vibrations shift towards a lower wavelength when sodium content increases.^[44] NFM_05 and NFM_15 show more non-symmetric cyanide stretching vibration peaks in RAMAN (Figure 3(b)), which can be ascribed to a higher tilt angle. Meanwhile, NFM_0 and NFM_10 show lower tilt and display similar peak profiles. Consequently, the A-site slide and octahedral tilt observed in the material are due to Mg-doping and changes in NFM water stoichiometry. The elemental quantification of the NFM samples was done by energy-dispersive X-ray Spectroscopy (EDS), with improved accuracy by using the $\text{Na}_4\text{Fe}(\text{CN})_6$ as the reference material. Table S6 shows the atomic ratios of Na: Fe, C:(Fe+Mg), and Mg: Fe obtained from EDS elemental quantification, and water (wt%) was

determined from TGA. Based on Table S6, the stoichiometric compound formulas were: $\text{Na}_{1.8}\text{Fe}[\text{Fe}(\text{CN})_{0.98}]_{0.02} \cdot 2.75\text{H}_2\text{O}$ for NFM_0, $\text{Na}_{1.82}\text{Mg}_{0.04}\text{Fe}_{0.92}[\text{Fe}(\text{CN})_6]_{0.99} \cdot 0.01 \cdot 2.48\text{H}_2\text{O}$ for NFM_05, $\text{Na}_{1.81}\text{Mg}_{0.05}\text{Fe}_{0.81}[\text{Fe}(\text{CN})_6]_{0.98} \cdot 0.02 \cdot 2.58\text{H}_2\text{O}$ for NFM_10 and $\text{Na}_{1.81}\text{Mg}_{0.13}\text{Fe}_{0.75}[\text{Fe}(\text{CN})_6]_{0.98} \cdot 0.02 \cdot 2.27\text{H}_2\text{O}$ for NFM_15.

The samples' morphology was cubic at a micrometer length scale using SEM (Figure S1)). Figure S1 (a) shows that NFM_0 has an average particle size of 1.1 μm , NFM_05 (Figure S1 (b)) has an average particle size of 1.21 μm . The NFM_10 (Figure S1 (c)) forms much smaller particles with an average particle size of 0.7 μm , and NFM_15 (Figure S1 (d)) forms an average particle size of 1.36 μm . A gradual increase in the particle size can be

observed with Mg-doping; however, NFM_10 deviates from this trend.

Figure 4. Shows high-resolution XPS spectra (Fe 2p) of (a) NFM_0, (b) NFM_05, (c) NFM_10, and (d) NFM_15. Meanwhile, high-resolution XPS spectra of Mg 2p were displayed in Figure S3. (a), (b), and (c) for NFM_05, NFM_10, and NFM_15, respectively. The XPS data was calibrated using C1s reference peak at 284.8 eV. The binding energies of all the samples have been summarized in Table S7. NFM_0, NFM_05, NFM_10, and NFM_15 show the binding energy of 707.12 eV, 706.33 eV, 704.66 eV, and 703.53 eV, respectively, for Fe^{II} 2P_{3/2} and 719.46 eV, 719.27 eV, 717.45 eV and 716.3 eV for Fe^{II} 2P_{1/2}. Additional peaks for NFM_0, NFM_05, NFM_10, and NFM_15 were observed at 709.91 eV, 708.65 eV, 708.22 eV, and 705.8 eV were assigned to the Fe^{III} 2P_{1/2} and the peaks observed at 722.04 eV, 721.86 eV, 719.89 eV and 719.2 eV were assigned to the Fe^{III} 2P_{3/2}, respectively.

A decreasing trend in the binding energy was observed with increased concentration of Mg²⁺ doping in NFM. Incorporating a lower electronegative element Mg (EN=1.31) for Fe (EN=1.83) increased the electron density around the Fe–C–N–Fe chain through the inductive effect, causing the increase in the bond length of C–N (observed in XRD refinement results, Table S5) reducing the binding energy. The 2p peak of Mg²⁺ is displayed in Figure S3 (a), (b) and (c) for NFM_05, NFM_10 and NFM_15, respectively. The peaks around

50.4 eV confirm the presence of Mg²⁺ in the NFM_05, NFM_10, and NFM_15, respectively.

The electrochemical performance of all the samples was evaluated using galvanostatic and CV methods. Figure 5(a) shows CV curve of NFM_0, NFM_05, NFM_10 and NFM_15. The NFM_0 shows the oxidation peaks at 3.09 V, 3.4 V, and 3.8 V and reduction peaks at 2.86 V, 3.31 V, 3.42 V, and 3.82 V. All the peaks are in agreement with previous reports.^[45–47] The Oxidation / Reduction of high spin (HS–Fe–N–C, 8c site) Fe³⁺/Fe²⁺ can be observed at 3.09 V/2.86 V. However, the oxidation/reduction of low spin (LS–Fe–C–N, 8c site) Fe³⁺/Fe²⁺ can be observed at 3.4 V/3.31 V and 3.82 V/3.42 V, respectively. The oxidation/reduction Fe³⁺/Fe²⁺ for NFM_05 was found to be (3.13 V, 3.46 V, 3.82 V, 4.02 V) / (2.66 V, 2.89 V, 3.27 V, 3.8 V). NFM_10 displays the oxidation/reduction Fe³⁺/Fe²⁺ at (3.05 V, 3.4 V, 3.81 V, 4.01 V/2.74 V, 2.97 V, 3.3 V, 3.78 V). The oxidation/reduction peak Fe³⁺/Fe²⁺ for NFM_15 was observed at (3.10 V, 3.44 V, 3.84 V, 4.01 V/2.68 V, 2.82 V, 3.29 V, 3.8 V). The change in the redox voltage for Mg-doped samples can be attributed to the charge-spin lattice coupling effect associated with lattice distortion.^[48] An additional oxidation peak was observed at 4 V in Mg-doped samples, and the intensity of the corresponding reduction peak due to the extraction of Na⁺ ions from 24 d sites, around 3.8 V, also increased.^[49] The additional extraction of sodium from 24 d sites is caused by promoting the oxidation/reduction of low spin Fe³⁺/Fe²⁺. The change in

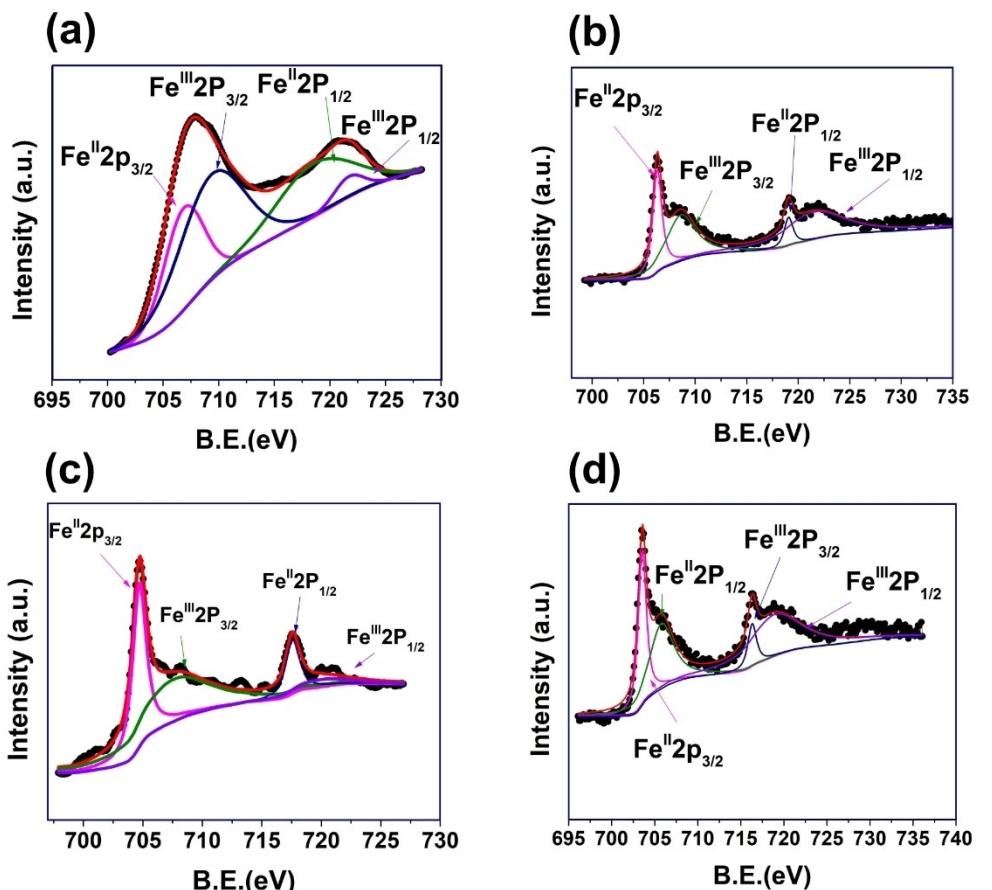


Figure 4. Fe 2p XPS spectra of (a) NFM_0, (b) NFM_05, (c) NFM_10, and (d) NFM_15.

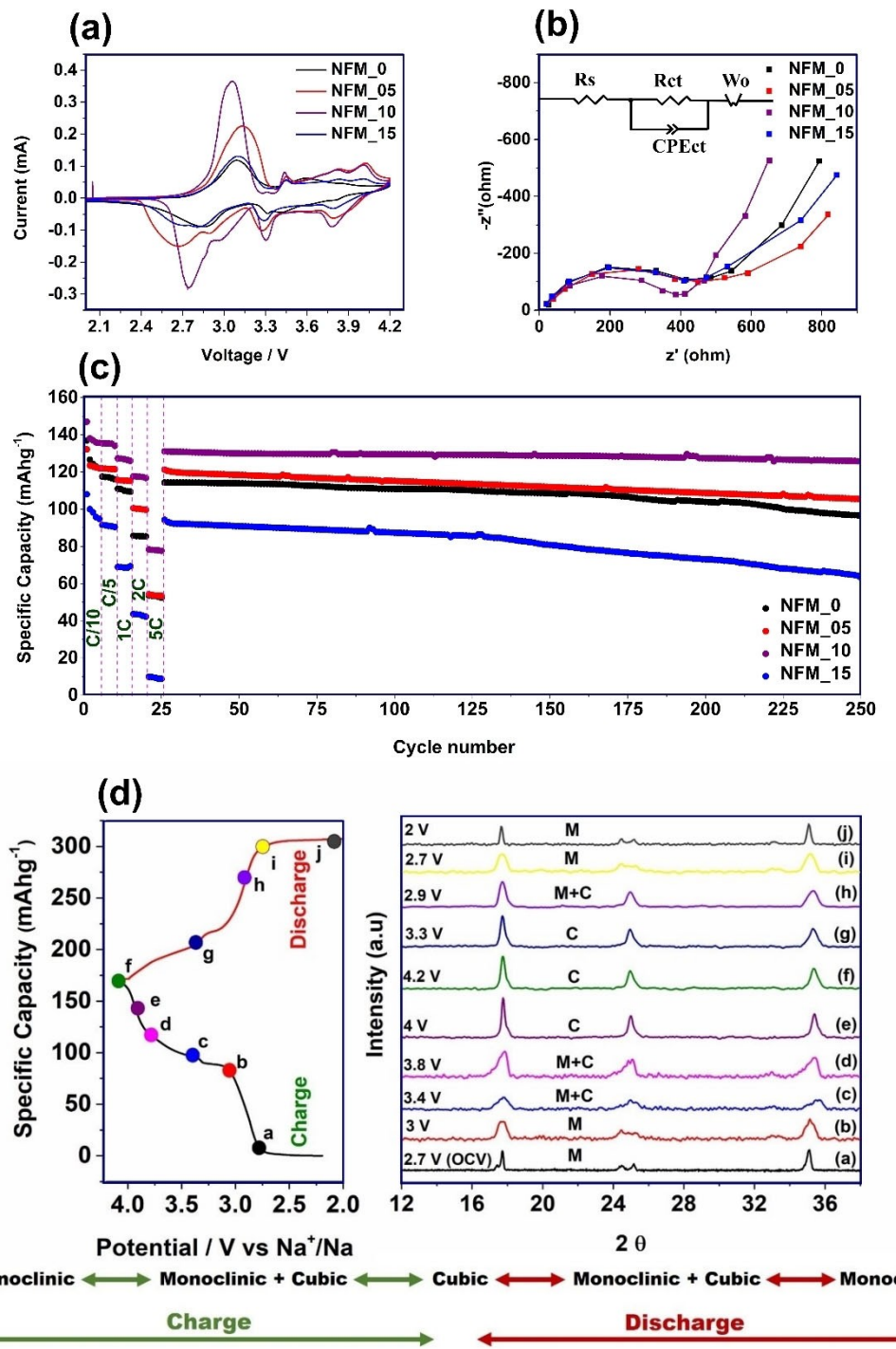


Figure 5. (a) CV Curves of NFM_0, NFM_05, NFM_10, and NFM_15, respectively, (b) EIS spectra of NFM samples after 1st cycle, (c) rate performance of NFM samples and long cycling (d) Ex Situ XRD pattern of NFM_10 at different voltages during the charge/discharge cycle.

octahedral tilt angle and the lesser volume expansion can be the responsible cause of the extraction of Na-ions from 24 d sites.

Figure S4 (a) shows that NFM_0 can deliver the reversible capacity of 127 mAhg $^{-1}$ and capacity retention of 69% after 250 cycles at a C/10 rate. The reversible capacity of NFM_05 was found to be 123 mAhg $^{-1}$ and capacity retention of 80% after 250 cycles at C/10 (Figure S4 (b)) (Figure 5(c)). NFM_10

(Figure S4 (c)) shows the improved reversible capacity of 138 mAhg $^{-1}$ and capacity retention of 85% after 250 cycles at a C/10 rate (Figure 5(c)). This improved performance can be obtained by optimized octahedral tilt and extraction of Na-ion from 24d sites, indicating the activation of additional LS-Fe. The electrochemical performance of NFM_15 fades rapidly on discharge, delivering only a reversible capacity of 100 mAhg $^{-1}$ (Figure S4 (d)) and retaining only 57% of the capacity after

250 cycles at a C/10 rate (Figure 5(c)). The higher octahedral tilt distortion can reduce the PBA lattice's micropores, inhibiting the Na-ion diffusion and contributing to the observed poor electrochemical performance. The rate performance of NFM_0, NFM_05, NFM_10, and NFM_15 were also evaluated at different current rates (Figure 5(c)) C/5, 1 C, 2 C, and 5 C, with NFM_10 delivering the best metrics at all C-rates. At 5 C NFM_0, NFM_05, NFM_10 and NFM_15 delivers the reversible capacities of 53 mAh g⁻¹, 53 mAh g⁻¹, 78 mAh g⁻¹ and 10 mAh g⁻¹ respectively. The improved reversible capacity at 5 C in NFM 10 can be attributed to enhanced diffusion channels caused by optimized octahedral tilts.

Transport kinetics of Na-ions were studied by Electrochemical Impedance Spectroscopy (EIS) (Figure 5(b)) measured for all the samples after the first charge-discharge cycle. The low-frequency Warburg region of the EIS spectra was used to quantify the diffusion of Na-ions by determining the Na-ion diffusion coefficient through the equation (5):^[50]

$$D = R^2 T^2 / 2 A^2 n^4 F^4 C^2 \sigma^2 \quad (5)$$

Where "R" is the gas constant, "T" is the absolute temperature, "A" is the surface area of the electrode, "n" is the number of electrons transferred per molecule during the redox reaction, F is the Faraday constant, "C" is the concentration Na-ion within the electrode and "σ" is the Warburg factor. The Warburg factor was calculated using the slope of plot $1/\omega^{1/2}$ vs Z' (Figure S5). The Na-ion diffusion constant was found to be 1.41×10^{-14} , 1.72×10^{-14} , 4.23×10^{-14} , and 1.25×10^{-14} for NFM_0, NFM_05, NFM_10, and NFM_15. NFM_10 shows the highest diffusion constant due to optimized octahedral tilts through Mg doping. However, the reduced diffusion in NFM_15 can be attributed to higher octahedral tilts, which inhibit the movements of Na-ion through the pores made from the -Fe-CN-Fe-NC- chain.^[16] The diffusion constant supports our assumption that optimizing octahedral tilts can improve the diffusion channels throughout the crystal. The EIS spectra of NFM samples were fitted using the equivalent circuit, as shown in Figure 5(b). The high-frequency intercept at the real axis represents the R_s caused by ohmic resistance from electrolyte and electrical contacts within the cell. The charge transfer resistance at the electrode-electrolyte interface is represented by R_{ct} (the broad semicircle region). The CPE_{ct} is used to represent the double-layer capacitor and the porous nature of the electrode results in the deviation from the ideal capacitor behavior. Therefore, a constant phase element (CPE_{ct}) is used. The straight line at the low-frequency region shows Warburg element W_o . The values of R_s and R_{ct} have been tabulated in Table S9. The R_{ct} for NFM_0, NFM_05, NFM_10, and NFM_15 was found to be 393.8 Ω, 383 Ω, 357.5 Ω, and 398 Ω respectively, as the trend shown by the diffusion coefficient values of the doped samples.

The charge storage mechanism in NFM_10 was investigated using ex-situ XRD (Figure 5(d)). At ~24.8°, the peaks corresponding to the (-211) and (211) planes are characteristic monoclinic phase peaks. (-211) and (211) planes start merging from 3.4 V charging, forming a biphasic state (monoclinic+cubic). The pure cubic phase was formed when NFM_10 was charged to

4 V, and the (-211) and (211) planes merged to form the (220) plane. The pure cubic phase was observed till the 3.3 V discharging state. At 2.9 V, a mixed (cubic+monoclinic) phase was found at the discharging state. The structure reversed back to the monoclinic phase after 2.7 V discharging states, which shows the reversibility of the charge/discharge process.

Conclusions

Optimizing the octahedral tilts can be crucial to the design of Prussian blue analogs (PBAs) as Na-ion battery cathodes. Understanding the distortion in PBAs is critical and demands a more fundamental understanding of designing high-performance cathodes for Na-ion batteries. Herein, the Goldschmidt tolerance factor was further improved and utilized in PBAs by considering the A-site's effective radius and the hydration effect, resulting in better distortion prediction. Incorporating electrochemically inert elements like Mg in PBAs can help tune the octahedral tilts and the distortion magnitudes. Mg doping and interstitial water can reduce the distortion magnitude, which can be predicted using the Goldschmidt tolerance factor. The refined octahedral tilt angle provides structural stability by reducing the distortion magnitude and improving diffusion kinetics, enhancing the specific capacity of the cathode by activation of additional low spin Fe by increasing the bond length of CN ligand, as Mg-doping increases the electron density around the -Fe-CN-Fe-N-C-Fe- chain through inductive effect. The optimized tilts can also improve the diffusion pathway, improving rate capability. The best electrochemical performance was obtained for optimized NFM_10 (10% Mg-doping), as further doping NFM_15 (15% Mg doping) affected the electrochemical performance due to a higher octahedral tilt angle. NFM_10 shows the improved reversible capacity of 138 mAh g⁻¹ and a reversible capacity retention of 85% after 250 cycles at a C/10 rate through optimized octahedral tilt and preferential extraction of Na-ion from 24d sites, indicating the activation of additional LS-Fe.

Conflict of Interests

The authors declare that they have no known competing financial interests or personal relationships that could have appeared to influence the work reported in this paper.

Data Availability Statement

The data that support the findings of this study are available from the corresponding author upon reasonable request.

Keywords: Prussian Blue analogs • Cathode Optimization • Mg-doping • Octahedral Tilt • Prussian White • Tilt engineering • Sodium Iron (II) Hexacyanoferrate • Na-ion Batteries • Sustainable Chemistry

- [1] Y. Gao, H. Zhang, J. Peng, L. Li, Y. Xiao, L. Li, Y. Liu, Y. Qiao, S. L. Chou, *Carbon Energy* 2024, 6, 1–43.
- [2] Z. Cui, S. Sun, G. Ning, L. Liang, Z. Wang, J. Qiao, L. Zhang, J. Chen, Z. Zhang, *J. Mater. Chem. A* 2024, 29335–29354.
- [3] Y. Xiao, J. Xiao, H. Zhao, J. Li, G. Zhang, D. Zhang, X. Guo, H. Gao, Y. Wang, J. Chen, G. Wang, H. Liu, *Small* 2024, 20, 1–22.
- [4] G. Oh, J. Kim, S. Kansara, H. Kang, H. G. Jung, Y. K. Sun, J. Y. Hwang, *J. Energy Chem.* 2024, 93, 627–662.
- [5] Z. Hao, X. Shi, Z. Yang, X. Zhou, L. Li, C. Q. Ma, S. Chou, *Adv. Mater.* 2024, 36, 1–30.
- [6] Z. Chen, Y. Deng, J. Kong, W. Fu, C. Liu, T. Jin, L. Jiao, *Adv. Mater.* 2024, 36, 1–27.
- [7] Z. Ahsan, Z. Cai, S. Wang, M. Moin, H. Wang, D. Liu, Y. Ma, G. Song, C. Wen, *Adv. Energy Mater.* 2024, 14, 1–31.
- [8] D. Das, S. Manna, S. Puravankara, *Batteries* 2023, 9, 10.3390/batteries9040193.
- [9] A. Tyagi, Nagmani, S. Puravankara, *Sustain. Energy Fuels* 2022, 6, 550–595.
- [10] M. S. Palaganas, J. S. Garcia, G. D. D. Sanglay, L. M. E. Sapanta, L. A. Limjoco, J. D. Ocon, *Batter Supercaps* 2024, 202400280, 10.1002/batt.202400280.
- [11] Y. Huang, M. Xie, J. Zhang, Z. Wang, Y. Jiang, G. Xiao, S. Li, L. Li, F. Wu, R. Chen, *Nano Energy* 2017, 39, 273–283.
- [12] Y. Yang, E. Liu, X. Yan, C. Ma, W. Wen, X.-Z. Liao, Z.-F. Ma, *J. Electrochem. Soc.* 2016, 163, A2117–A2123.
- [13] Y. You, X. L. Wu, Y. X. Yin, Y. G. Guo, *Energy Environ. Sci.* 2014, 7, 1643–1647.
- [14] W. Li, Z. Wang, F. Deschler, S. Gao, R. H. Friend, A. K. Cheetham, *Nat. Rev. Mater.* 2017, 2, 10.1038/natrevmats.2016.99.
- [15] H. L. B. Boström, A. L. Goodwin, *Acc. Chem. Res.* 2021, 54, 1288–1297.
- [16] J. Cattermull, M. Pasta, A. L. Goodwin, *Mater. Horiz.* 2021, 8, 3178–3186.
- [17] H. L. B. Boström, A. B. Cairns, M. Chen, D. Daisenberger, C. J. Ridley, N. P. Funnell, *Chem. Sci.* 2024, 15, 3155–3164.
- [18] J. Cattermull, N. Roth, S. J. Cassidy, M. Pasta, A. L. Goodwin, *J. Am. Chem. Soc.* 2023, 145, 24249–24259.
- [19] J. Cattermull, K. Sada, K. Hurlbutt, S. J. Cassidy, M. Pasta, A. L. Goodwin, *Chem. Mater.* 2022, 34, 5000–5008.
- [20] A. Regueiro, J. Castells-Gil, C. Shen, I. Mikulska, C. Allen, L. Bogani, R. Torres-Cavanillas, *Mater Adv* 2024, 7473–7480.
- [21] J. Y. Heo, J. H. Lee, G. Kim, H. Kim, H. J. Lee, J. H. Lee, *Adv. Funct. Mater.* 2024, 2409171, 1–9.
- [22] D. M. Kim, Y. Kim, D. Arumugam, S. W. Woo, Y. N. Jo, M. S. Park, Y. J. Kim, N. S. Choi, K. T. Lee, *ACS Appl. Mater. Interfaces* 2016, 8, 8554–8560.
- [23] J. H. Lee, J. G. Bae, M. S. Kim, J. Y. Heo, H. J. Lee, J. H. Lee, *ACS Nano* 2024, 18, 1995–2005.
- [24] F. M. Maddar, D. Walker, T. W. Chamberlain, J. Compton, A. S. Menon, M. Copley, I. Hasa, *J. Mater. Chem. A* 2023, 11, 15778–15791.
- [25] W. R. Brant, R. Mogensen, S. Colbin, D. O. Ojwang, S. Schmid, L. Häggström, T. Ericsson, A. Jaworski, A. J. Pell, R. Younesi, *Chem. Mater.* 2019, 31, 7203–7211.
- [26] N. A. Benedek, C. J. Fennie, *Phys. Rev. Lett.* 2011, 106, 10.1103/PhysRevLett.106.107204.
- [27] Y. Xu, J. Wan, L. Huang, M. Ou, C. Fan, P. Wei, J. Peng, Y. Liu, Y. Qiu, X. Sun, C. Fang, Q. Li, J. Han, Y. Huang, J. A. Alonso, Y. Zhao, *Adv. Energy Mater.* 2019, 9, 10.1002/aenm.201803158.
- [28] J. Cattermull, M. Pasta, A. L. Goodwin, *J. Am. Chem. Soc.* 2023, DOI 10.1021/jacs.3c08752.
- [29] G. Kieslich, S. Sun, A. K. Cheetham, *Chem. Sci.* 2015, 6, 3430–3433.
- [30] B. Xie, P. Zuo, L. Wang, J. Wang, H. Huo, M. He, J. Shu, H. Li, S. Lou, G. Yin, *Nano Energy* 2019, 61, 201–210.
- [31] B. Xie, L. Wang, J. Shu, X. Zhou, Z. Yu, H. Huo, Y. Ma, X. Cheng, G. Yin, P. Zuo, *ACS Appl. Mater. Interfaces* 2019, 11, 46705–46713.
- [32] W. Wang, Y. Gang, Z. Hu, Z. Yan, W. Li, Y. Li, Q. F. Gu, Z. Wang, S. L. Chou, H. K. Liu, S. X. Dou, *Nat. Commun.* 2020, 11, 1–9.
- [33] H. L. B. Boström, J. A. Hill, A. L. Goodwin, *Phys. Chem. Chem. Phys.* 2016, 18, 31881–31894.
- [34] J. H. Lee, N. C. Bristowe, J. H. Lee, S. H. Lee, P. D. Bristowe, A. K. Cheetham, H. M. Jang, *Chem. Mater.* 2016, 28, 4259–4266.
- [35] H. L. B. Boström, W. R. Brant, *J. Mater. Chem. C* 2022, 10, 13690–13699.
- [36] V. M. Goldschmidt, *Naturwissenschaften* 1926, 14, 477–485.
- [37] R. D. Shannon, *Acta Crystallogr. Sect. A* 1976, 32, 751–767.
- [38] M. Lucero, D. B. Armitage, X. Yang, S. K. Sandstrom, M. Lyons, R. C. Davis, G. E. Sterbinsky, N. Kim, D. M. Reed, X. Ji, X. Li, Z. Feng, *ACS Appl. Mater. Interfaces* 2023, 15, 36366–36372.
- [39] P. Xiao, J. Song, L. Wang, J. B. Goodenough, G. Henkelman, *Chem. Mater.* 2015, 27, 3763–3768.
- [40] J. Song, L. Wang, Y. Lu, J. Liu, B. Guo, P. Xiao, J. J. Lee, X. Q. Yang, G. Henkelman, J. B. Goodenough, *J. Am. Chem. Soc.* 2015, 137, 2658–2664.
- [41] C. M. Kareis, S. H. Lapidus, J. H. Her, P. W. Stephens, J. S. Miller, *J. Am. Chem. Soc.* 2012, 134, 2246–2254.
- [42] L. Yang, Q. Liu, M. Wan, J. Peng, Y. Luo, H. Zhang, J. Ren, L. Xue, W. Zhang, *J. Power Sources* 2020, 448, 227421.
- [43] H. L. B. Boström, W. R. Brant, *J. Mater. Chem. C* 2022, 10, 13690–13699.
- [44] X. Tang, H. Liu, D. Su, P. H. L. Notten, G. Wang, *Nano Res.* 2018, 11, 3979–3990.
- [45] Y. Lu, L. Wang, J. Cheng, J. B. Goodenough, *Chem. Commun.* 2012, 48, 6544–6546.
- [46] J. C. Pramudita, S. Schmid, T. Godfrey, T. Whittle, M. Alam, T. Hanley, H. E. A. Brand, N. Sharma, *Phys. Chem. Chem. Phys.* 2014, 16, 24178–24187.
- [47] Y. Liu, Y. Qiao, W. Zhang, Z. Li, X. Ji, L. Miao, L. Yuan, X. Hu, Y. Huang, *Nano Energy* 2015, 12, 386–393.
- [48] J. Song, L. Wang, Y. Lu, J. Liu, B. Guo, P. Xiao, J. J. Lee, X. Q. Yang, G. Henkelman, J. B. Goodenough, *J. Am. Chem. Soc.* 2015, 137, 2658–2664.
- [49] C. Yan, A. Zhao, F. Zhong, X. Feng, W. Chen, J. Qian, X. Ai, H. Yang, Y. Cao, *Electrochim. Acta* 2020, 332, 135533.
- [50] H. Fu, C. Liu, C. Zhang, W. Ma, K. Wang, Z. Li, X. Lu, G. Cao, *J. Mater. Chem. A* 2017, 5, 9604–9610.

Version of record online: March 18, 2025